JACS
JOURNAL OF THE AMERICAN CHEMICAL SOCIETY
pubs.acs.org/JACS
Article

Herzberg Type-I or Type-II Predissociation Dynamics at the Conical Intersection: Bifurcation into Adiabatic or Nonadiabatic Pathway

Kyung Chul Woo and Sang Kyu Kim*

Cite This: J. Am. Chem. Soc. 2025, 147, 19851−19858

Read Online

ACCESS | Metrics & More | Article Recommendations | Supporting Information

ABSTRACT: Bifurcation dynamics into Herzberg type-I and type-II predissociation pathways at the conical intersection have been characterized in terms of their distinct reaction rates and energy-disposal dynamics from the picosecond time-resolved product state distributions measured at multiple S_1/S_2 vibronic states of thioanisole ($C_6H_5SCH_3$). Electronic predissociation (type-I) occurs on a faster time scale and leads to the larger translational energies being released to the fragments ($C_6H_5S^{\bullet}$ + $^{\bullet}CH_3$) compared to the vibrational predissociation (type-II). While type-II dominates at the S_1 zero-point level, the type-I quantum yield increases sharply near the S_1/S_2 conical intersection, which is consistent with the striking dynamic resonance observed for the reactive flux in the proximity of the conical intersection. Nonadiabatic product yield at the asymptotic limit was found to be enhanced predominantly through the type-I channel, suggesting that the quantum-mechanical nature of the reactive flux prepared near the first S_1/S_2 conical intersection is likely to be retained at the second S_0/S_2 conical intersection encountered in the later stage as there is little time to be altered during the ultrafast S-CH_3 bond extension on the repulsive potential energy curve linking two conical intersections, enabling nonadiabatic control over product yields through the state-selection of the reactive flux.

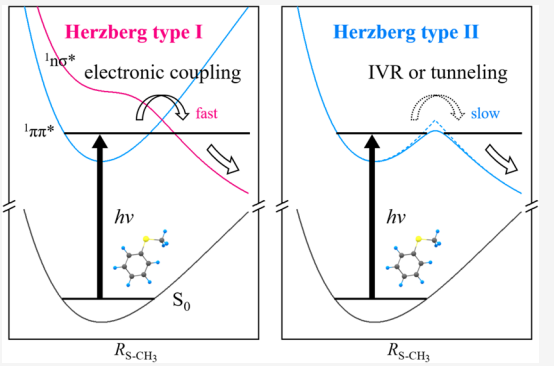

INTRODUCTION

The Born−Oppenheimer approximation (BOA)[1] has long been a cornerstone in our understanding of chemical reaction dynamics, successfully describing nuclear motions during chemical transformations where nuclear motion is governed by adiabatic potential energy surfaces. This approximation has been especially effective in the study of ground-state unimolecular reactions. However, when it comes to excited-state reactions, the Born−Oppenheimer approximation becomes less reliable due to the close proximity of multiple excited states, leading to the likelihood of nonadiabatic transitions. These transitions occur when the reactive flux switches between different adiabatic potential energy surfaces during the reaction, a phenomenon most prevalent at conical intersections—points where two or more electronic states become degenerate at the same molecular conformation. For polyatomic molecular systems, the conical intersection exists on a complex, multidimensional seam (defined by the gradient and coupling vector coordinates), which significantly complicates the task of fully understanding the dynamics, especially when curve crossings occur along the reaction pathway. In this context, the predissociation of polyatomic molecules in excited states represents a prototypical system, where reaction outcomes are heavily influenced by the characteristics of conical intersections. This process has been seminally classified by Herzberg into two distinct pathways: Type-I and Type-II predissociation.[2] Type-I, also referred to as electronic predissociation, involves a nonadiabatic transition where the reactive flux switches between potential energy surfaces. In contrast, Type-II, or vibrational predissociation, occurs when the flux remains on the same adiabatic potential energy surface throughout the reaction.

A key system for exploring excited-state predissociation and nonadiabatic transitions is $\pi\sigma^*$-mediated photodissociation of heteroaromatic molecules such as phenol,[3−15] thiophenol,[16−27] anisole,[28] or thioanisole.[29−36] These molecules serve as model systems for studying the dynamics of conical intersections. In these molecules, the first electronically excited state (S_1) is bound ($\pi\pi^*$), and is optically bright in the S_1−S_0 transition. Upon excitation, the S_1 state is crossed by the higher-lying S_2 state ($n\sigma^*$), which is repulsive along the C_6H_5X-Y (X = O, N, or S; Y = H, D, or CH_3) chemical bond extension coordinate. Importantly, while the S_2 state is optically dark, the mixing between S_1 and S_2 states becomes significant, especially near the conical intersection between the two states.

Received: March 6, 2025
Revised: May 20, 2025
Accepted: May 22, 2025
Published: May 26, 2025

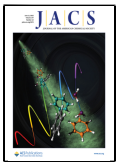

Downloaded via KOREA ADVANCED INST SCI AND TECHLGY on July 18, 2025 at 09:23:15 (UTC).
See https://pubs.acs.org/sharingguidelines for options on how to legitimately share published articles.

© 2025 American Chemical Society

https://doi.org/10.1021/jacs.5c03968
J. Am. Chem. Soc. 2025, 147, 19851−19858

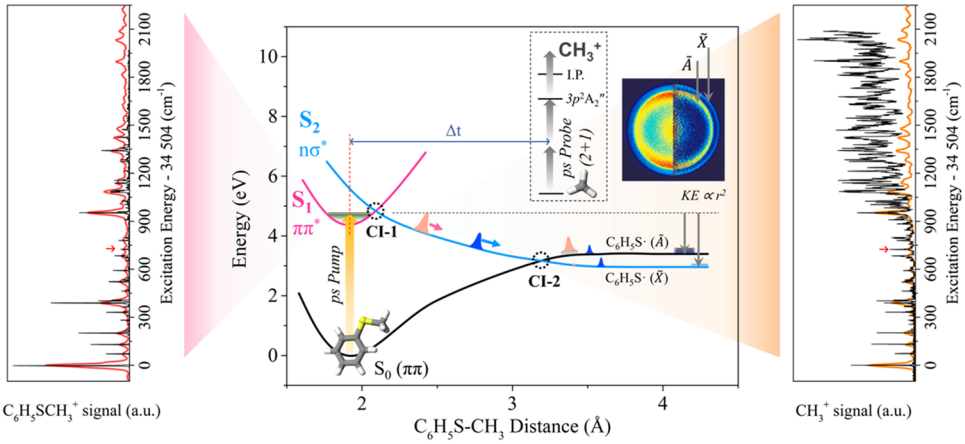

Figure 1. Schematic of the electronic potential energy surfaces of thioanisole along the S-CH_3 bond elongation coordinate. Experimental scheme for the ps time-resolved velocity-map CH_3^+ ion imaging was depicted. The inset shows the fragment image[29] taken at the 722 cm^{-1} dynamic resonance, giving two distinct rings. R2PI (left) and PHOFEX (right) spectra taken with the ps (red) or ns (black) laser pulse from the S_1−S_0 spectral origin to 2300 cm^{-1} region are shown with small red arrows at the 722 cm^{-1} vibronic mode. The wavepacket taking the Herzberg type-I (blue) or type-II (orange) is riding on the repulsive part of the diabatic S_2 state.

For thioanisole ($C_6H_5SCH_3$), as depicted in Figure 1, the S_1 state (A′) is bound, while the S_2 state (A″) is repulsive along the S-CH_3 bond elongation coordinate. It should be noted that the three lowest singlet states, S_0, S_1, and S_2, referenced throughout this manuscript, are described in the diabatic representation. In this framework, each state is assumed to retain its characteristic electronic configuration throughout the entire reaction pathway, regardless of any curve crossings. At the planar geometry where the S-CH_3 bond axis is aligned with the phenyl ring, the S_1/S_2 conical intersection (CI-1) lies near the S_1 minimum energy geometry, which can be accessed within the Franck−Condon window of the S_1−S_0 transition. The excited-state reactive flux, initially generated by the S_1−S_0 transition, must traverse or circumvent CI-1, guided by forces arising from the derivatives of the potential energy surfaces with respect to nuclear coordinates, before interacting with the repulsive diabatic S_2 state. As the reaction progresses, the flux encounters the S_0/S_2 conical intersection (CI-2), where the flux bifurcates, leading to two possible outcomes: one following an adiabatic path to the $C_6H_5S^\bullet$ ($\tilde{A}$) radical, and the other following a nonadiabatic path to the $C_6H_5S^\bullet$ ($\tilde{X}$) radical. The key insight here is that the relative yields of these two products can be determined by the translational energy distributions of the nascent CH_3 fragments. Notably, the translational energy distribution allows for the precise estimation of the relative yields of the two distinct product channels, with a small energetic difference (~3000 cm^{-1} or 8.6 kcal/mol)[37] between the $C_6H_5S^\bullet$ ($\tilde{A}$) and $C_6H_5S^\bullet$ ($\tilde{X}$) fragments. This small energy difference makes it possible to experimentally measure the nonadiabatic transition probability (P_{NA}) at CI-2. The relative yield of the $C_6H_5S^\bullet$ ($\tilde{X}$) fragment—obtained from the integrated intensity of the outer ring in the velocity-map ion images—can thus provide a direct measure of P_{NA}, which is proportional to the nonadiabatic transition probability at CI-2. Through this approach, we can obtain a quantitative understanding of the nonadiabatic transition dynamics and gain precise insights into the bifurcated reaction pathways governing excited-state predissociation. By exploring the complex reaction dynamics at conical intersections in this system, we not only gain a deeper understanding of excited-state chemistry but also offer a direct experimental method to probe nonadiabatic processes in polyatomic systems, advancing the broader field of nonadiabatic reaction dynamics.

RESULTS AND DISCUSSION

In the two-color resonance-enhanced two-photon ionization (R2PI) spectrum of the jet-cooled thioanisole, a number of the S_1 vibronic bands have been well identified in the frequency-domain.[29] It is noteworthy that the photofragment excitation (PHOFEX) spectrum taken by monitoring the $^\bullet CH_3$ (v = 0) fragment as a function of the excitation energy of the nanosecond (ns) laser pulse demonstrated that individual bands of R2PI or PHOFEX are correlated quite well with 1:1 correspondences in the low internal energy region. It should be noted that the nascent $^\bullet CH_3$ fragment may also be vibrationally excited, particularly in its low-frequency bending mode. However, probing such a vibrationally excited $^\bullet CH_3$ (v = 1) is not expected to yield dynamical information significantly different from that obtained by probing $^\bullet CH_3$ in its ground vibrational state, especially since the vibrational excitation of $^\bullet CH_3$ is unlikely to result from an impulsive force at the conical intersection, implying that the rather simple energetic shift (~1.7 ± 0.2 kcal/mol) is expected for the translation energy distribution measured from $^\bullet CH_3$ (v = 1) compared to that from $^\bullet CH_3$ (v = 0).[29] With increasing the S_1 internal energy (E_{int}) above ~1000 cm^{-1}, however, the R2PI signals are found to be diminished whereas PHOFEX signals persist and get congested at the same time (Figure 1), suggesting that the reaction rate may increase rapidly beyond the corresponding energy region. The S−CH_3 bond dissociation channel mostly takes the adiabatic pathway at the CI-2 in the 0−2000 cm^{-1} range of the S_1 internal energy (E_{int}), as indicated in the experimentally estimated P_{NA} which remains more or less at ~0.1 over the whole energy region. Most remarkably, however, the nonadiabatic transition probability is strongly enhanced at the vibrational mode of ~722 cm^{-1} to give P_{NA} ~ 0.3, as previously reported.[29,30] This striking dynamic resonance of the nonadiabatic transition probability[29] has been subject to intensive theoretical[38−41] and experimental[30,32,34] investigations in recent years. Although the whole dynamical details seem to be still beyond thorough understanding, direct access to the proximity of the CI-1 via the 722 cm^{-1} mode

https://doi.org/10.1021/jacs.5c03968
J. Am. Chem. Soc. 2025, 147, 19851−19858

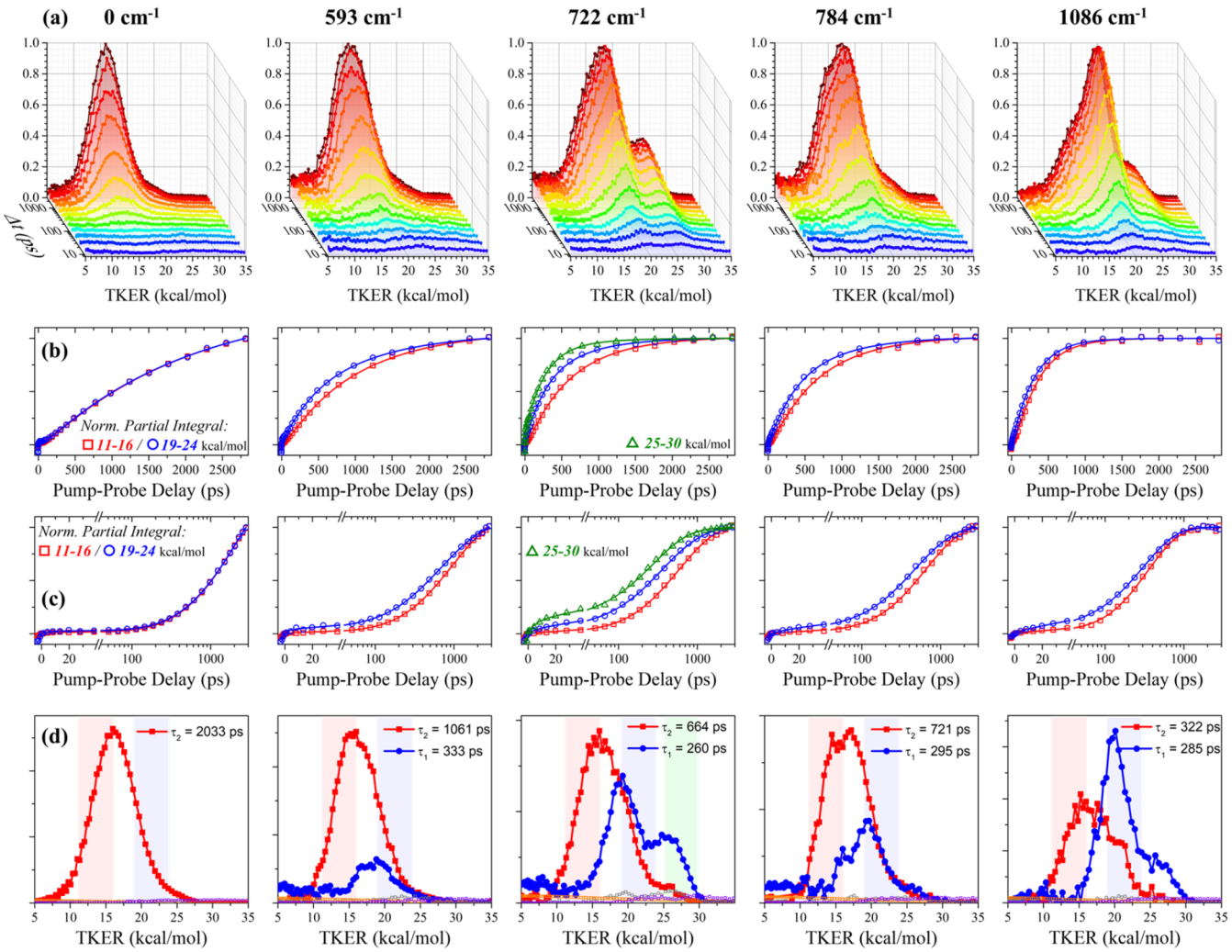

Figure 2. Time-resolved product total translational energy distributions. (a) Total kinetic energy release (TKER) distributions extracted from the time-resolved velocity-map CH_3^+ images at selected S_1 vibronic levels (see the Supporting Information for full data set of all other S_1 vibronic levels). (b) Transients for the appearance of the fragment intensity integrated over the low KE region (11−16) kcal/mol; red squares; shaded reddish in (d) and those in the high KE region (19−24) kcal/mol; blue circles; shaded bluish in (d). For the result at 722 cm^{-1}, the transient integrated over the higher KE region (25−30) kcal/mol; green triangles; shaded greenish in (d) is additionally shown. For the comparison of temporal profiles of two components in the 0−2.8 ns range, the transients are normalized to the same intensity scale. (c) Transients displayed in the logarithmic scale. While the low KE and high KE transients match perfectly at the S_1 zero-point-level (ZPL), they show distinct temporal dynamics for all other S_1/S_2 vibronic levels studied here. Thus, the multicomponent global analysis has been carried out for all transients (see the text). (d) The contribution of the type-II (red filled squares) and that of the type-I (blue filled circles) could be clearly separated out from the global analysis. Note that there are two distinct KE distributions responsible for the $C_6H_5S^\bullet$ ($\tilde{A}$) fragment, whereas the higher KE distribution associated with $C_6H_5S^\bullet$ ($\tilde{X}$) stands out only at 722 cm^{-1}. For the details of the global analysis method, including how minor contributions (open symbols) are treated, see the Supporting Information.

(asymmetric C−S−C stretching) excitation should be responsible for such a pronounced nonadiabatic dynamic resonance. Experimental efforts were made to look into this unique dynamic resonance features in the time-domain using the femtosecond (fs) transient spectroscopy.[30] And yet, neither the P_{NA} enhancements nor the dissociation rate changes could be observed primarily due to intrinsic energy-time uncertainty of the fs laser pulse. In our previous report,[34] picosecond (ps) pump−probe spectroscopy was employed to fulfill all the requirements of frequency and temporal resolutions for the comprehensive real-time state-specific dynamics. Bifurcation of the reactive flux at CI-1 was proposed from the experimental finding that the rate of the nonadiabatic channel producing $C_6H_5S^\bullet$ ($\tilde{X}$) is significantly faster than that of the adiabatic channel giving the $C_6H_5S^\bullet$ ($\tilde{A}$) fragment. Nevertheless, the previous work[34] was confined to the excitation of the 722 cm^{-1} mode (S_1) only, and as such, it did not fully address the complexities of nonadiabatic dynamics. In this study, we present a comprehensive investigation across a wide excitation energy range, revealing for the first time that the bifurcation into Herzberg type-I and type-II predissociation channels is robust across all S_1/S_2 vibronic bands. This provides deeper insights into the nonadiabatic dynamical behavior of the reactive flux near the conical intersection. Time-resolved product state distributions, measured for individual S_1/S_2 vibrational bands, reveal previously obscured mechanisms of bifurcation between nonadiabatic and adiabatic pathways at the conical intersection. Furthermore, it is noteworthy that the experimental results have been significantly enhanced and refined, featuring unbiased, high-contrast fragment ion images

https://doi.org/10.1021/jacs.5c03968
J. Am. Chem. Soc. 2025, 147, 19851−19858

and effective elimination of multiphoton background effects, among other improvements (see details below).

The experimental works on partially deuterated thioanisoles (C_6H_5S-CD_3, C_6H_5S-CHD_2, or C_6H_5S-CH_2D)[31,33] revealed that the P_{NA} enhancement is not confined to the 722 cm^{-1} mode. Rather, it is significantly enhanced for any normal modes along which the diabatic potential energy surfaces of S_2 are unbound, while the S_1/S_2 crossing points are located near the S_1 minimum. Consequently, the CI-1 nuclear configuration can be accessed by one quantum of the corresponding vibrational mode excitation. From diabatic perspective, this also suggests that the excited vibronic band must exhibit strong coupling to the reaction coordinate, as its normal mode displacement should be at least partially aligned with the S-CH_3 extension coordinate. Indeed, the S_1/S_2 potential energy curves constructed with respect to the one-dimensional normal-mode displacement, effectively rationalized the mode-dependent behavior of P_{NA}.[31,33] Specifically, the phase space accessed by a given vibronic transition should be close to the CI-1, both in terms of position and momentum, allowing the corresponding reactive flux to funnel through the CI-2 with an enhanced likelihood of yielding a strong P_{NA} enhancement. Since the P_{NA} enhancement results from the nonadiabatic transition at the CI-2, these experimental findings suggest a strong correlation between CI-1 and CI-2 in terms of their dynamic properties (vide infra).

Once the reactive flux was prepared in the vicinity of the S_1/S_2 conical intersection by the particular vibronic transition, it may be followed by two distinct predissociation channels of type-I or type-II. Since vibronic coupling mechanisms involved in deriving two different electronic and vibrational predissociation reactions are anticipated to be quite different in nature, dynamic outputs from the type-I and type-II pathways are also expected to be quite distinct in terms of reaction rates, product yields, or the energy disposal dynamics. Accordingly, from the picosecond time-resolved photofragment translational energy distributions (Figure 2), the dynamic outputs resulting either from the type-I or type-II predissociation could be unambiguously separated out for all the individual S_1/S_2 vibronic transitions. The translational energies of the products are expected to be larger, and the product appearance rate is anticipated to be faster in type-I predissociation compared to type-II predissociation. This difference arises because the reactive flux in type-II predissociation explores a larger vibrational phase-space volume as it searches for the adiabatic minimum energy path during vibrational predissociation for the Lissajous motion. As a result, this leads to lower kinetic energies (KE) and higher internal energies for the fragments. In contrast, during type-I predissociation, the reactive flux funnels through the conical intersection, where the corresponding phase-space should be narrowly confined within the curve-crossing region. This naturally results in larger translational energies and smaller internal energies for the fragments. Consequently, the bifurcation ratio of type-I to type-II at the CI-1 can be precisely determined from the ratio of the total intensity of the faster-rising high-KE component to the slower-rising low-KE component in the full product state distribution. At the S_1 zero-point level (ZPL) of thioanisole, the translational energy distribution of the products shows a single component, both in terms of its appearance rate ($\tau_2 \sim 2033$ ps) and the Gaussian-shaped translational energy distribution, which peaks at ~16 kcal/mol with a full width at half-maximum (FWHM) of ~5 kcal/mol, as shown in Figure 2. This suggests that the S-CH_3 bond cleavage occurs exclusively on the adiabatic potential energy surface via type-II vibrational predissociation at the S_1 ZPL. Notably, vibronic excitation at the S_1 ZPL primarily leads to the $C_6H_5S^{\bullet}$ ($\tilde{A}$) product at the asymptotic limit, implying that the reactive flux taking the type-II vibrational predissociation path likely follows the adiabatic path at CI-2 as well.

However, as the excitation energy increases, the translational energy distribution of the products becomes asymmetrically broadened, exhibiting two distinct temporal profiles. At a 593 cm^{-1} band excitation, for example, the temporal evolution of the low-KE component (11−16 kcal/mol) of the translational energy distribution differs significantly from that of the high-KE component (19−24 kcal/mol). Global analyses of the time-resolved product state distributions (see the Supporting Information for details) reveal that the faster-rising component, with $\tau_1 \sim 333$ ps and a larger translational energy distribution peaking at ~19 kcal/mol, can be distinctly separated from the slower-rising component ($\tau_2 \sim 1061$ ps) with a smaller translational energy distribution peaking at ~16 kcal/mol. The relative quantum yield of the former is estimated to be ~23%, indicating that the type-I electronic predissociation channel plays a significant role at such a low vibrational energy of 593 cm^{-1}, although type-II vibrational predissociation remains dominant. It is remarkable that the contribution of type-I predissociation (albeit small) is even observable at an S_1 internal energy of 69 cm^{-1} (Figure 3), suggesting that the S_1/S_2 vibronic mixing begins very early in the Franck−Condon window. It is important to note, however, that an increase in the type-I contribution does not necessarily

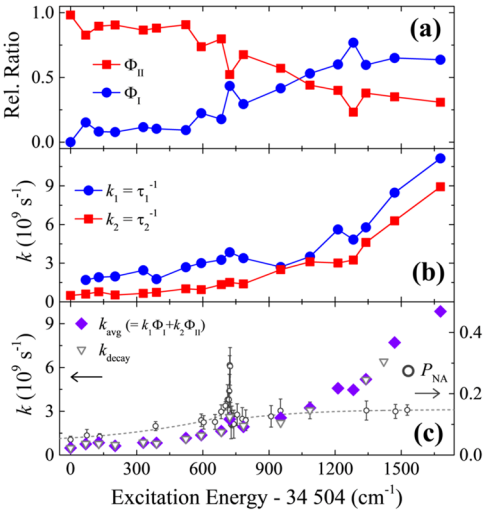

Figure 3. Branching ratios and rates of the Herzberg type-I and type-II predissociation reactions. (a) Quantum yields of the Herzberg type-I (Φ_I, blue circles) and type-II (Φ_{II}, red squares) versus the S_1 internal energy. (b) Rate constants of the Herzberg type-I (Φ_I, blue circles) and type-II (Φ_{II}, red squares) versus the S_1 internal energy extracted from the global analyses. (c) Rate constants taken from the parent ion transients[34] (k_{decay}, inverse triangles) perfectly match with those obtained from the weighted averages of the type-I and type-II rates ($k_1\Phi_I + k_2\Phi_{II}$, filled diamonds). The previously reported P_{NA}[29] is plotted for the comparison (right axis). Note that the P_{NA} in ref 29 was obtained from the $\tilde{X}/\tilde{A}$ product branching ratio from the total kinetic energy distributions. The nonadiabatic transition probability at CI-2 from the type-I predissociation channel only should be higher (see the text).

https://doi.org/10.1021/jacs.5c03968
J. Am. Chem. Soc. 2025, 147, 19851−19858

favor the nonadiabatic channel at CI-2. As seen in the P_{NA} (Figure 3c), there is minimal enhancement of the nonadiabatic transition probability at 593 cm^{-1}, which remains low in this energy region.

One can estimate the bifurcation ratio of the nonadiabatic (type-I) to adiabatic (type-II) channels at CI-1 from the two temporally and energetically distinct components of the product state distribution. In contrast, the product branching ratio of $C_6H_5S^{\bullet}$ ($\tilde{X}$) relative to $C_6H_5S^{\bullet}$ ($\tilde{A}$) results from the nonadiabatic transition probability at CI-2. While there is no direct linear correlation between the nonadiabatic bifurcation ratios at CI-1 and CI-2, it is important to note that the final $\tilde{X}/\tilde{A}$ product branching ratio (or P_{NA}) is predominantly enhanced by the type-I component (Figure 2). This strongly suggests that the reactive flux funneled through CI-1 via electronic predissociation has a higher probability of following the nonadiabatic path at CI-2, leading to the $C_6H_5S^{\bullet}$ ($\tilde{X}$) product. Interestingly, this phenomenon is qualitatively consistent with the semiclassical view of the Landau−Zener equation,[42,43] which posits that a faster, quantum-mechanically narrower reactive flux (as seen in the type-I predissociation pathway) should have a higher probability of undergoing a nonadiabatic transition. Although the dynamic details of nonadiabatic transitions at conical intersections remain somewhat ambiguous, this suggests that the proximity of the reactive flux to CI-1 plays a crucial role in determining the nonadiabatic transition probability at CI-2. This is particularly relevant because the structural properties of the reactive flux at CI-2 are expected to be similar to those at CI-1, with the main difference being a slightly elongated S-CH_3 bond length, as the two are connected by the repulsive diabatic $n\sigma^*$ state.

In other words, although nonadiabatic transitions at CI-2 generally become more probable as the contribution of type-I predissociation at CI-1 increases, they are not resonantly enhanced unless the quantum nature of the reactive flux is close to that of the conical intersection. Meanwhile, the reactive flux that follows the vibrational adiabatic path (type-II) is more widely spread out in terms of nuclear configuration, particularly along the degrees of freedom orthogonal to the reaction coordinate. This makes it more likely to take the adiabatic path at CI-2, predominantly leading to the $C_6H_5S^{\bullet}$ ($\tilde{A}$) product.

As the excitation energy increases further, the relative bifurcation ratio of type-I (Φ_I) exhibits a monotonic increase, though with some fluctuation and slight mode dependence. Specifically, Φ_I increases to approximately 0.4 at an excitation energy (E_{int}) of ∼953 cm^{-1} and to ∼0.6 at E_{int} ∼ 1340 cm^{-1} (Figure 3). This trend supports the idea that eigenstates above the S_1/S_2 conical intersection are more likely to be accessed as the excitation energy increases. Consequently, the type-I predissociation path—where quantum states in the upper adiabat transit to those in the lower adiabat in some sense—becomes more probable. It is important to note that the reactive flux, which is prepared by excitation of a particular vibronic mode, may, depending on its position and momentum, return to the diabatic S_1 state with finite probability, thus following the vibrational predissociation path. Overall, the reaction rate for type-I predissociation is faster than that of type-II predissociation. Interestingly, the type-II predissociation rate increases more rapidly with increasing internal energy of S_1 compared to the type-I rate (Figure 3). For instance, as the internal energy increases from 593 to 1086 cm^{-1}, k_2 increases by more than a factor of 3 (from 0.94×10^9 to 3.11×10^9 s^{-1}), whereas the corresponding increase in k_1 over the same energy range is relatively small (from 3.00×10^9 to 3.51×10^9 s^{-1}). For the vibrational predissociation channel, if it becomes statistical in nature, the reaction rate is expected to be proportional to the number of quantum states at the transition state ($N^{\ddagger}$), according to the RRKM theory. This helps explain the rapid increase of the type-II reaction rate, as $N^{\ddagger}$ increases steeply with rising internal energy above the barrier along the adiabatic reaction path beneath the conical intersection. In contrast, the energy-dependent behavior of the type-I reaction rate is less straightforward. This rate is strongly influenced by the vibronic coupling strengths between the two diabatic states, though it is also expected to increase as the number of coupling paths rises with increasing excitation energy. However, it is crucial to emphasize that the bifurcation dynamics at the CI-1, in terms of the rates and branching ratios for type-I and type-II predissociation pathways, reflect the chaotic characteristics of the conical intersection. This means that the bifurcation dynamics cannot be explained by simple, kinetically competitive processes involving one-way transitions from a single reactant species. If such processes were the case, the product appearance rate would match the reactant disappearance rate, independent of the kinetic energy of the products.

The reactive flux in the S_1/S_2 state either directly rides on the repulsive diabatic S_2 (leading to the high KE product) or detours the conical intersection to explore the large phase space to find the minimum-energy nonplanar adiabatic path[40] or possibly along the multidimensional conical intersection seam coordinates (giving the low KE product). The S_1/S_2 coupling and subsequent predissociation paths are quantum mechanical in nature, and thus the experiment could not be rationalized by a simple kinetic scheme. In the meantime, it is noteworthy that the product transient cannot be fit with a single exponential rising function, more evidently for the lower KE region where the vibrational predissociation prevails, Figure 3. The product yield in such transients somewhat remains more or less constant for an induction period of tens of ps prior to its exponential rise according to the predissociation reaction rate. The delayed-appearance of the product yield suggests that there might exist an intermediate particularly along the vibrational predissociation pathway where the fragment translational energy is relatively low. Namely, the reactive flux might be 'trapped' for a certain period of time before it is finally produced out. This remains somewhat puzzling and constitutes an open question. One possible explanation is that the flux traveling along the repulsive diabatic S_2 surface—potentially distributed over many degrees of freedom orthogonal to the reaction coordinate—might become momentarily trapped on the upper adiabatic surface upon reaching the vicinity of CI-2, particularly within the more complex vibrational predissociation pathway.[44]

Interestingly, the type-I quantum yield shows a rather sharp increase in the 700−800 cm^{-1} energy range, suggesting that the S_1/S_2 state mixing may become significant in this energy range (Figure 3). This observation aligns with the experimental finding of nonadiabatic dynamic resonance at 722 cm^{-1} in terms of energetics, although the energetic coincidence is necessary but not sufficient for the reactive flux to be near the conical intersection, given the multidimensional nature of the system. As Tully has clearly explained,[45] the reactive flux (or wavepacket) that is closer to the conical intersection in its

https://doi.org/10.1021/jacs.5c03968
J. Am. Chem. Soc. 2025, 147, 19851−19858

nuclear configuration (in the multidimensional potential energy surfaces) has a higher probability of undergoing a nonadiabatic transition. Thus, the strong enhancement of P_{NA} at 722 cm^{-1} indicates that the nuclear configuration accessed by this mode excitation is near CI-1 along its projection onto the corresponding normal mode coordinate. More importantly, this also implies that CI-2 should closely resemble CI-1 in terms of nuclear configuration for the reactive flux prepared by the 722 cm^{-1} mode. That is, the reactive flux prepared by excitation in the 722 cm^{-1} band near CI-1 maintains a nuclear configuration that is also close to CI-2, except for a slightly elongated S−CH_3 bond length, resulting in a large enhancement of the $\tilde{X}/\tilde{A}$ product branching ratio. In addition to the strong dynamic resonance at 722 cm^{-1}, it is noteworthy that the P_{NA} value increases slowly but monotonically from 0.06 to 0.13 in the 0−1500 cm^{-1} range. This can be attributed to the increase in type-I quantum yield with increasing excitation energy (as discussed above).

Importantly, it should be emphasized that the experimental results in this work were confined within the Franck−Condon window. Specifically, only in-plane vibrational modes of the S_1 thioanisole are predominantly prepared in the optical transition, preventing exploration of nonplanar nuclear configurations in the excited state. As the conical intersection lies on the (3N-8)-dimensional seam coordinates, multiple dynamic resonant enhancements of the nonadiabatic transition probability may occur. However, at high internal energies, the optically prepared zeroth modes are expected to be randomized due to the rapid intramolecular vibrational redistribution (IVR), and nonadiabatic dynamics are not anticipated to be resonantly enhanced at any specific mode excitation thereafter.

CONCLUSIONS

Herein, the otherwise ambiguous Herzberg type-I and type-II predissociation pathways could be clearly identified and separated based on their temporal and energy-disposal dynamics for the first time in this work. Specifically, from the picosecond time-resolved product state distributions measured at various S_1/S_2 vibronic bands of jet-cooled thioanisole, the Herzberg type-I (electronic predissociation) or type-II (vibrational predissociation) pathway bifurcating at the conical intersection can be distinguished by their distinct temporal and kinetic-energy profiles of the products. The predissociation rate for type-I is found to be faster than for type-II, while the translational energies of the fragments are larger in the former than in the latter. In other words, the reactive flux undergoing the nonadiabatic transition at the S_1/S_2 conical intersection (type-I) moves faster, resulting in fragments with larger translational but smaller internal energies. In contrast, the reactive flux following the vibrational predissociation path (type-II) moves slower on the adiabatic potential energy surfaces, leading to fragments with smaller translational but larger internal energies. The quantum yield of type-I increases sharply in the 700−800 cm^{-1} energy range, suggesting that the S_1/S_2 conical intersection is likely located in this energy region, where many nearby quantum states in the upper adiabat can be accessed with high probability. This supports the previously reported striking dynamic resonance in the nonadiabatic transition probability at the 722 cm^{-1} mode excitation, as it is likely that the quantum state corresponding to the 722 cm^{-1} mode resides near the S_1/S_2 conical intersection. It was found that the increase in type-I quantum yield at CI-1 does not necessarily lead to an increase in nonadiabatic transition probability at CI-2. However, the nonadiabatic product yield at the asymptotic limit is primarily enhanced by the type-I predissociation channel. The nonadiabatic transition at CI-2, which determines the final product branching ratio, is likely governed by the proximity to the conical intersection, both in terms of the position and momentum of the reactive flux. The reactive flux prepared near CI-1 is more likely to be close to CI-2 in the electronic predissociation process, as the quantum mechanical nature of the reactive flux has little time to change during the ultrafast elongation of the S-CH_3 bond on the repulsive potential curve connecting two closely spaced conical intersections at the planar geometry. This experimental study provides an ideal platform for further sophisticated experiments and theoretical calculations aimed at a thorough understanding of the nonadiabatic dynamics occurring near conical intersections in many aspects.

EXPERIMENTAL METHODS

Experimental procedures of the ps time-resolved velocity map imaging were described elsewhere,[14,15,27,46] and only a brief overview is given. Starting from the 1 kHz synchronized fs/ps Ti:sapphire regenerative amplifier system (Legend Elite-USP/P, Coherent), pump/probe pulses with tunable ultraviolet wavelengths were obtained by the nonlinear mixing from the independent optical parametric amplifiers (TOPAS-800 ps, Light Conversion) pumped by the half-split fundamental outputs. Pump pulse was used for the specific S_1/S_2 vibronic excitation of thioanisole in the supersonic jet ($T_{rot} \sim 1K$), whereas the probe laser pulse at 333.5 nm was given with the delay time ranging from −20 ps to 2.81 ns to detect the nascent $^{\bullet}CH_3$ fragment in real-time. Pump and probe pulses were colinearly aligned and focused onto the molecular beam using plano-convex spherical lenses. Polarizations of both laser pulses were parallel with the detector. The thioanisole (Sigma-Aldrich) sample heated at 80 °C was mixed with the neon carrier gas before it is supersonically expanded (Even-Lavie valve) into vacuum by the backing pressure of 2 bar with the repetition rate of 200 Hz. The molecular beam was collimated through a 2 mm diameter skimmer prior to the overlap with laser pulses. The ions were accelerated in the velocity-map ion imaging[47] setup equipped with the position sensitive detector. Ion spots on a phosphor screen were captured by a triggered CMOS camera (GS3-U3−32S4, PointGrey). The higher repetition rate of the Even-Lavie pulsed valve as well as the faster frame rate of the camera sensor, employed in this work, have facilitated data acquisition of the ps time-resolved fragment ion images. Compared to the previous measurements given in ref 34., the experimental data here are much improved and refined because of several factors including (1) the colder rotational temperature of the molecular beam, (2) the faster data acquisition to give the larger set of time delay positions, (3) event-counting mode image acquisition which is advantageous for unbiased detector gain and better image resolutions, and (4) the little contribution of the multiphoton background by using the less intense laser pulses. Thus, more reliable data of higher signal-to-noise ratio at faster acquisition rate is achieved for the experiment, enabling more detailed global analysis.

ASSOCIATED CONTENT

Supporting Information

The Supporting Information is available free of charge at https://pubs.acs.org/doi/10.1021/jacs.5c03968.

Kinetic energy release at the origin and 722 cm^{-1} band, delayed appearance of low kinetic energy region; generalized bifurcation dynamics; details in the revised global analysis; and full data sets of ps time-resolved velocity map CH_3^+ imaging (PDF)

https://doi.org/10.1021/jacs.5c03968
J. Am. Chem. Soc. 2025, 147, 19851−19858

AUTHOR INFORMATION

Corresponding Author

Sang Kyu Kim − *Department of Chemistry, KAIST, Daejeon 34141, Republic of Korea;* orcid.org/0000-0003-4803-1327; Email: sangkyukim@kaist.ac.kr

Author

Kyung Chul Woo − *Department of Chemistry, KAIST, Daejeon 34141, Republic of Korea;* Present Address: Combustion Research Facility, Sandia National Laboratories, Livermore, California 94551, United States; orcid.org/0000-0002-9387-9397

Complete contact information is available at: https://pubs.acs.org/10.1021/jacs.5c03968

Notes

The authors declare no competing financial interest.

ACKNOWLEDGMENTS

This work was supported by the National Research Foundation of Korea under Project Numbers RS-2023-00208926, RS-2024-00436153, and 2019R1A6A1A10073887. The authors thank Min Seok Kang and Dr. Junggil Kim for their helpful assistance.

REFERENCES

(1) Born, M.; Oppenheimer, R. Zur Quantentheorie der Molekeln. *Ann. Phys.* **1927**, *389* (20), 457−484.

(2) Herzberg, G. Molecular spectra and molecular structure. In *Electronic spectra and electronic structure of polyatomic molecules*; Van Nostrand, 1966; Vol. 3.

(3) Sobolewski, A. L.; Domcke, W.; Dedonder-Lardeux, C.; Jouvet, C. Excited-state hydrogen detachment and hydrogen transfer driven by repulsive $^1\pi\sigma^*$ states: A new paradigm for nonradiative decay in aromatic biomolecules. *Phys. Chem. Chem. Phys.* **2002**, *4* (7), 1093−1100.

(4) Tseng, C. M.; Lee, Y. T.; Ni, C. K. H atom elimination from the $\pi\sigma^*$ state in the photodissociation of phenol. *J. Chem. Phys.* **2004**, *121* (6), 2459−2461.

(5) Nix, M. G. D.; Devine, A. L.; Cronin, B.; Dixon, R. N.; Ashfold, M. N. R. High resolution photofragment translational spectroscopy studies of the near ultraviolet photolysis of phenol. *J. Chem. Phys.* **2006**, *125* (13), No. 133318.

(6) Tseng, C.-M.; Lee, Y. T.; Lin, M.-F.; Ni, C.-K.; Liu, S.-Y.; Lee, Y.-P.; Xu, Z. F.; Lin, M. C. Photodissociation Dynamics of Phenol. *J. Phys. Chem. A* **2007**, *111* (38), 9463−9470.

(7) Nix, M. G. D.; Devine, A. L.; Dixon, R. N.; Ashfold, M. N. R. Observation of geometric phase effect induced photodissociation dynamics in phenol. *Chem. Phys. Lett.* **2008**, *463* (6), 305−308.

(8) Iqbal, A.; Pegg, L.-J.; Stavros, V. G. Direct versus Indirect H Atom Elimination from Photoexcited Phenol Molecules. *J. Phys. Chem. A* **2008**, *112* (39), 9531−9534.

(9) King, G. A.; Oliver, T. A. A.; Nix, M. G. D.; Ashfold, M. N. R. High Resolution Photofragment Translational Spectroscopy Studies of the Ultraviolet Photolysis of Phenol-d_5. *J. Phys. Chem. A* **2009**, *113* (28), 7984−7993.

(10) Roberts, G. M.; Chatterley, A. S.; Young, J. D.; Stavros, V. G. Direct Observation of Hydrogen Tunneling Dynamics in Photoexcited Phenol. *J. Phys. Chem. Lett.* **2012**, *3* (3), 348−352.

(11) Lee, C.; Lin, Y.-C.; Lee, S.-H.; Lee, Y.-Y.; Tseng, C.-M.; Lee, Y.-T.; Ni, C.-K. Advantage of spatial map ion imaging in the study of large molecule photodissociation. *J. Chem. Phys.* **2017**, *147* (1), No. 013904.

(12) Lin, Y.-C.; Lee, C.; Lee, S.-H.; Lee, Y.-Y.; Lee, Y. T.; Tseng, C.-M.; Ni, C.-K. Excited-state dissociation dynamics of phenol studied by a new time-resolved technique. *J. Chem. Phys.* **2018**, *148* (7), No. 074306.

(13) Lai, H. Y.; Jhang, W. R.; Tseng, C.-M. Communication: Mode-dependent excited-state lifetime of phenol under the S_1/S_2 conical intersection. *J. Chem. Phys.* **2018**, *149* (3), No. 031104.

(14) Woo, K. C.; Kim, S. K. Multidimensional H Atom Tunneling Dynamics of Phenol: Interplay between Vibrations and Tunneling. *J. Phys. Chem. A* **2019**, *123* (8), 1529−1537.

(15) Woo, K. C.; Kim, J.; Kim, S. K. Conformer-Specific Tunneling Dynamics Dictated by the Seam Coordinate of the Conical Intersection. *J. Phys. Chem. Lett.* **2021**, *12*, 1854−1861.

(16) Lim, J. S.; Lim, I. S.; Lee, K.-S.; Ahn, D.-S.; Lee, Y. S.; Kim, S. K. Intramolecular Orbital Alignment Observed in the Photodissociation of [D_1]Thiophenol. *Angew. Chem., Int. Ed.* **2006**, *45* (38), 6290−6293.

(17) Lim, I. S.; Lim, J. S.; Lee, Y. S.; Kim, S. K. Experimental and theoretical study of the photodissociation reaction of thiophenol at 243 nm: Intramolecular orbital alignment of the phenylthiyl radical. *J. Chem. Phys.* **2007**, *126* (3), No. 034306.

(18) Devine, A. L.; Nix, M. G. D.; Dixon, R. N.; Ashfold, M. N. R. Near-Ultraviolet Photodissociation of Thiophenol. *J. Phys. Chem. A* **2008**, *112* (39), 9563−9574.

(19) Ashfold, M. N. R.; Devine, A. L.; Dixon, R. N.; King, G. A.; Nix, M. G. D.; Oliver, T. A. A. Exploring nuclear motion through conical intersections in the UV photodissociation of phenols and thiophenol. *Proc. Natl. Acad. Sci. U.S.A.* **2008**, *105* (35), No. 12701.

(20) Lim, J. S.; Lee, Y. S.; Kim, S. K. Control of intramolecular orbital alignment in the photodissociation of thiophenol: conformational manipulation by chemical substitution. *Angew. Chem., Int. Ed.* **2008**, *47* (10), 1853−1856.

(21) Lim, J. S.; Choi, H.; Lim, I. S.; Park, S. B.; Lee, Y. S.; Kim, S. K. Photodissociation Dynamics of Thiophenol-d_1: The Nature of Excited Electronic States along the S−D Bond Dissociation Coordinate. *J. Phys. Chem. A* **2009**, *113* (39), No. 10410.

(22) Oliver, T. A. A.; King, G. A.; Tew, D. P.; Dixon, R. N.; Ashfold, M. N. R. Controlling electronic product branching at conical intersections in the UV photolysis of *para*-substituted thiophenols. *J. Phys. Chem. A* **2012**, *116* (51), No. 12444.

(23) Venkatesan, T. S.; Ramesh, S. G.; Lan, Z.; Domcke, W. Theoretical analysis of photoinduced H-atom elimination in thiophenol. *J. Chem. Phys.* **2012**, *136* (17), No. 174312.

(24) You, H. S.; Han, S.; Lim, J. S.; Kim, S. K. ($\pi\pi^*/\pi\sigma^*$) Conical Intersection Seam Experimentally Observed in the S−D Bond Dissociation Reaction of Thiophenol-d_1. *J. Phys. Chem. Lett.* **2015**, *6* (16), 3202−3208.

(25) Ovejas, V.; Fernández-Fernández, M.; Montero, R.; Longarte, A. On the ultrashort lifetime of electronically excited thiophenol. *Chem. Phys. Lett.* **2016**, *661*, 206−209.

(26) Kim, J.; Woo, K. C.; Kim, K. K.; Kim, S. K. $\pi\sigma^*$-Mediated Nonadiabatic Tunneling Dynamics of Thiophenols in S_1: The Semiclassical Approaches. *J. Phys. Chem. A* **2022**, *126* (51), 9594−9604.

(27) Woo, K. C.; Kim, S. K. Real-Time Tunneling Dynamics through Adiabatic Potential Energy Surfaces Shaped by a Conical Intersection. *J. Phys. Chem. Lett.* **2020**, *11* (16), 6730−6736.

(28) Hadden, D. J.; Williams, C. A.; Roberts, G. M.; Stavros, V. G. Time-resolved velocity map imaging of methyl elimination from photoexcited anisole. *Phys. Chem. Chem. Phys.* **2011**, *13* (10), 4494−4499.

(29) Lim, J. S.; Kim, S. K. Experimental probing of conical intersection dynamics in the photodissociation of thioanisole. *Nat. Chem.* **2010**, *2*, 627−632.

(30) Roberts, G. M.; Hadden, D. J.; Bergendahl, L. T.; Wenge, A. M.; Harris, S. J.; Karsili, T. N. V.; Ashfold, M. N. R.; Paterson, M. J.; Stavros, V. G. Exploring quantum phenomena and vibrational control in σ^* mediated photochemistry. *Chem. Sci.* **2013**, *4* (3), 993−1001.

(31) Han, S.; Lim, J. S.; Yoon, J. H.; Lee, J.; Kim, S. Y.; Kim, S. K. Conical intersection seam and bound resonances embedded in

continuum observed in the photodissociation of thioanisole-d_3. *J. Chem. Phys.* **2014**, *140* (5), No. 054307.
(32) Wenge, A. M.; Karsili, T. N. V.; Rodriguez, J. D.; Cotterell, M. I.; Marchetti, B.; Dixon, R. N.; Ashfold, M. N. R. Tuning photochemistry: substituent effects on $\pi\sigma^*$ state mediated bond fission in thioanisoles. *Phys. Chem. Chem. Phys.* **2015**, *17* (25), No. 16246.
(33) Kim, S. Y.; Lee, J.; Kim, S. K. Conformer specific nonadiabatic reaction dynamics in the photodissociation of partially deuterated thioanisoles (C_6H_5S-CH_2D and C_6H_5S-CHD_2). *Phys. Chem. Chem. Phys.* **2017**, *19* (29), No. 18902.
(34) Woo, K. C.; Kang, D. H.; Kim, S. K. Real-Time Observation of Nonadiabatic Bifurcation Dynamics at a Conical Intersection. *J. Am. Chem. Soc.* **2017**, *139* (47), No. 17152.
(35) Lim, J. S.; You, H. S.; Kim, S.-Y.; Kim, S. K. Experimental observation of nonadiabatic bifurcation dynamics at resonances in the continuum. *Chem. Sci.* **2019**, *10* (8), 2404−2412.
(36) Lee, H.; Kim, S.-Y.; Kim, S. K. Multidimensional Characterization of the Conical Intersection Seam in the Normal Mode Space. *Chem. Sci.* **2020**, *11*, 6856−6861.
(37) Kim, J. B.; Yacovitch, T. I.; Hock, C.; Neumark, D. M. Slow photoelectron velocity-map imaging spectroscopy of the phenoxide and thiophenoxide anions. *Phys. Chem. Chem. Phys.* **2011**, *13* (38), No. 17378.
(38) Li, S. L.; Xu, X.; Hoyer, C. E.; Truhlar, D. G. Nonintuitive Diabatic Potential Energy Surfaces for Thioanisole. *J. Phys. Chem. Lett.* **2015**, *6* (17), 3352−3359.
(39) Li, S. L.; Truhlar, D. G. Full-dimensional multi-state simulation of the photodissociation of thioanisole. *J. Chem. Phys.* **2017**, *147* (4), No. 044311.
(40) Li, S. L.; Truhlar, D. G. Full-dimensional ground- and excited-state potential energy surfaces and state couplings for photodissociation of thioanisole. *J. Chem. Phys.* **2017**, *146* (6), No. 064301.
(41) Shu, Y.; Truhlar, D. G. Improved potential energy surfaces of thioanisole and the effect of upper surface variations on the product distribution upon photodissociation. *Chem. Phys.* **2018**, *515* (14), 737−743.
(42) Landau, L. Zur Theorie der Energieubertragung. II. *Phys. Z. Sowjetunion* **1932**, *2*, No. 46.
(43) Zener, C. Non-adiabatic crossing of energy levels. *Proc. R. Soc. London, Ser. A* **1932**, *137* (833), 696−702.
(44) Chatterley, A. S.; Roberts, G. M.; Stavros, V. G. Timescales for adiabatic photodissociation dynamics from the $\tilde{A}$ state of ammonia. *J. Chem. Phys.* **2013**, *139* (3), No. 034318.
(45) Tully, J. C. Perspective: Nonadiabatic dynamics theory. *J. Chem. Phys.* **2012**, *137* (22), No. 22A301.
(46) Woo, K. C.; Kim, S. K. Mode-specific Excited-state Dynamics of *N*-Methylpyrrole. *Phys. Chem. Chem. Phys.* **2019**, *21* (26), No. 14387.
(47) Eppink, A. T. J. B.; Parker, D. H. Velocity map imaging of ions and electrons using electrostatic lenses: Application in photoelectron and photofragment ion imaging of molecular oxygen. *Rev. Sci. Instrum.* **1997**, *68* (9), 3477−3484.

https://doi.org/10.1021/jacs.5c03968
J. Am. Chem. Soc. 2025, 147, 19851−19858